ACS Photonics

Article

Cite This: ACS Photonics 2017, 4, 2782-2788

pubs.acs.org/journal/apchd5

Near-Infrared and Optical Beam Steering and Frequency Splitting in Air-Holes-in-Silicon Inverse Photonic Crystals

Anna C. Tasolamprou,*[,†] Thomas Koschny,[‡] Maria Kafesaki,[†,¶] and Costas M. Soukoulis[†,‡]

[†]Institute of Electronic Structure and Laser, FORTH, 71110, Heraklion, Crete, Greece

[‡]Ames Laboratory and Department of Physics and Astronomy, Iowa State University, Ames, Iowa 50011, United States

[¶]Department of Materials Science and Technology, University of Crete, 71003, Heraklion, Crete, Greece

ABSTRACT: We present the design of a dielectric inverse photonic crystal structure that couples line-defect waveguide propagating modes into highly directional beams of controllable directionality. The structure utilizes a triangular lattice made of air holes drilled in an infinitely thick Si slab, and it is designed for operation in the near-infrared and optical regime. The structure operation is based on the excitation and manipulation of dark dielectric surface states, in particular on the tailoring of the dark states' coupling to outgoing radiation. This coupling is achieved with the use of properly designed external corrugations. The structure adapts and matches modes that travel through the photonic crystal and the free space. Moreover it facilitates the steering of the outgoing waves, is found to generate well-defined, spatially and spectrally isolated beams, and may serve as a frequency splitting component designed for operation in the near-infrared regime and in particular the telecom optical wavelength band. The design complies with the state-of-the-art Si nanofabrication technology and can be directly scaled for operation in the optical regime.

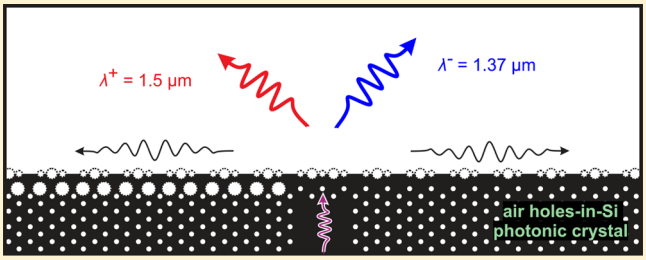

KEYWORDS: *photonic crystals, dielectric media, surface states, directional emission, frequency splitting, beam steering*

Dielectric photonic crystals are the electromagnetic wave analogue of electronic semiconductors.[1] They consist of periodically alternating regions of different dielectric materials that allow the modification of the electromagnetic wave dispersion properties.[2−4,9] Photonic crystal structures are theoretically infinite structures; however, when it comes to actual implementations, their size is in fact finite. The finite size gives rise to various additional phenomena that depend on the interfaces of the photonic crystal regions and the surrounding environment. One of the phenomena related to the finite size is the appearance of surface states, also known as surface modes (see for example ref 5) that propagate bound to the interface of the dielectric photonic crystals and the external space, similarly to the surface plasmon polaritons found at the metal−dielectric interfaces at high frequencies.[5−8] For many years, photonic crystal surface states have been generally treated as a subsidiary effect. Surface states on photonic crystals are dark states, meaning that they cannot couple directly to free-space propagating waves because the surface wave vector cannot be matched. In the past decade a surface plasmon polariton related experiment revealed an interesting potential for exploiting these dark states. In particular it has been demonstrated that surface plasmon polaritons can be used to enhance and control the collimation and directionality of the electromagnetic energy that exits a subwavelength metallic slit surrounded by side corrugations.[9−13] The work on the metallic slits inspired a series of investigations into the manipulation of the dielectric photonic crystal surface states and their role in shaping the electromagnetic energy that results from a dielectric photonic crystal-based structure. As a result, it has been found that the termination of the photonic crystal structure can be designed to provide desired surface wave dispersion properties,[14−17] while an additional corrugation can undertake the coupling of the dark surface states to outgoing radiation. The mechanism has been employed, among others, to sustain the collimation of free-space traveling beams,[18,19] to produce and control near-field focusing effects,[20,21] and to decrease the π angular spread, or 2π for a solid angle in 3D, of a forward-propagating beam that exits a subwavelength photonic crystal waveguide operating in the microwave and optical regime.[22−26] Moreover, in the case of the microwave regime and the corresponding high dielectric rods in air photonic crystals, it has been shown both theoretically and experimentally that the angle of the beam's directionality can be tuned by properly designing the terminating corrugations.[27,28] The frequency-dependent bend of the beams provides steering and frequency splitting capabilities, and consequently the manipulation of the dielectric, ohmic-loss-free, surface waves may be used in a variety of applications involving free-space coupling, as for example in demultiplexer components for optical communications, optical spectroscopy, and sensor applications.[29−32]

In this work we present the design of a dielectric photonic crystal-based frequency splitting and beam steering component

Received: July 12, 2017
Published: September 28, 2017

DOI: 10.1021/acsphotonics.7b00739
ACS Photonics 2017, 4, 2782−2788

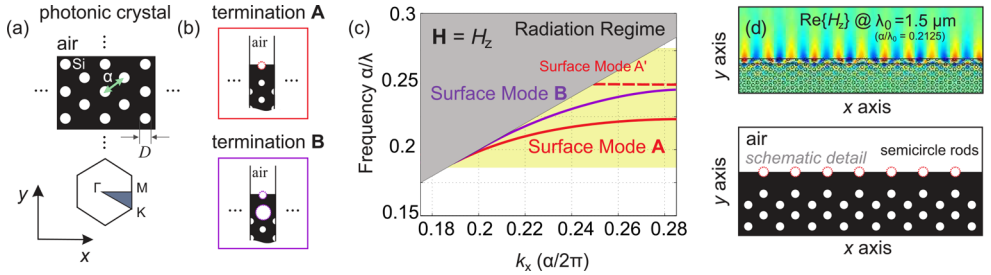

Figure 1. (a) Schematic of the infinite two-dimensional photonic crystal, which is the basic structural element of the photonic component discussed here. It consists of circular air rods of diameter D = 188 nm drilled in an infinite silicon slab with permittivity ε = 11.6. The photonic crystal arrangement is triangular, and the lattice constant is α = 320 nm. (b) Schematic of the supercell termination used for sustaining the surface modes, **A** (red frame) and **B** (purple frame). (c) Dispersion diagram of the supported surface modes for terminations **A** (red curves) and **B** (purple curve). The polarization is **H** = H_z. Red solid line corresponds to the acoustic surface mode for the termination **A**, and red dashed line corresponds to the optical, nearly flat surface mode for termination **A**. Purple solid line corresponds to the sole surface mode supported by termination **B**. The shaded yellow area corresponds to the photonic band gap of the structure. (d) Field distribution of the real part of the H_z component of the field in an infinitely wide (along x) photonic crystal with termination **A**, at λ_0 = 1.5 μm (α/λ_0 = 0.2125), and corresponding structure schematic.

for operation in the near-infrared regime and in particular the telecom optical band, ranging from 1260 to 1625 nm. Employing air-holes-in-bulk-dielectric design rather than the most forward dielectric-rods-in-air approach enables the fabrication of photonic structures that can be more easily scaled to infrared and optical wavelengths. Si-based, ohmic-loss-free, frequency splitting components operating in these short wavelengths are of high interest for application in optical nanocircuitry. Recent works have demonstrated the development of silicon waveguide-based demultiplexers,[33] all-dielectric multilayered ring structures for beam collimation and steering,[34] and all-dielectric asymmetric dimers for tunable directional scattering.[35] In a similar way, our structure provides control over the direction of the energy that emanates from optical components made of dielectric air-holes-in-Si photonic crystals, which, to our knowledge, has not been demonstrated yet. The advantage of using photonic crystals for controlling the free-space outgoing beams is that, apart from achieving the aforementioned operations, it enables the communication between the mature Si-based photonic crystal optical circuits and the outside world in a natural manner.

Our component consists of a line-defect waveguide that feeds the bulk photonic crystal termination, which is properly designed to sustain surface modes. Additional, properly aligned, scatterers are used to couple the dark surface waves to radiation modes. We have already validated experimentally the principle of operation for the dielectric-rods-in-air complementary structure in the microwave regime.[28] However, due to fabrication constraints, this geometry is ill suited for applications in the near-infrared and optical regime. In order to scale the structure down for operation in shorter wavelengths, a photonic crystal geometry consisting of air holes in a bulk dielectric material is a better candidate for fabrication. We also take into account the available materials and the current fabrication feasibility in the near-infrared and optical regime. For the existence of well-defined, wide band gaps the materials involved should exhibit high refractive index contrast (one of the materials is air). Materials such as TiO_2, GaAs, $Al_xGa_{1-x}As$, and Si exhibit sufficiently high permittivity at the infrared and optical regime, and at the same time they have practically no losses below their band edges.[36−39] As far as the fabrication of the components at these wavelengths is concerned, CMOS-compatible methods, such as ion beam etching, allow the creation of void air pores in Si and the creation of inverse photonic crystals with lattice constants on the order of hundreds of nanometers.[40−42] Consequently, we choose to investigate a two-dimensional structure (of infinite thickness) that is considered to be made of a Si slab perforated with air holes in a triangular arrangement and provides directionality control in the horizontal plane. In the second subsection we present the details of the structure and dispersion properties of its surface states. In the third subsection we present the evaluation of the structure as a beam steering and frequency splitting component in the infrared regime. The component can be directly scaled down for operation in the optical regime. Moreover the present design could be used as a preliminary investigation for the extension to the widely investigated three-dimensional Si-based inverse woodpiles[43,44] with the possibility of beam shaping and directionality control in both the horizontal and vertical plane.

Dielectric Dark State Manipulation. We present the design of an air-holes-in-Si inverse photonic crystal-based structure that controls the directionality of the energy emanating from a line-defect photonic crystal waveguide. The operation is based on the excitation and manipulation of dark, surface propagation modes. The structural element of our steering component is the bulk, dielectric photonic crystal schematically shown in Figure 1a. It consists of an infinitely thick silicon slab where circular air holes are drilled in a two-dimensional standard triangular lattice arrangement. The lattice constant is equal to α = 320 nm, and the diameter of the air cylinders (holes) is equal to D = 188 nm; the permittivity of the silicon is equal to ε = 11.6. We choose to use the triangular lattice arrangement and TM polarization with the principal field component **H** = H_z. TM polarization is proven to provide wider band gaps in such photonic crystal structures.[45] The photonic crystal exhibits a full photonic band gap within the range α/λ = [0.183, 0.276] or λ = [1.15 μm, 1.74 μm]; that is, the band gap spans the range of the optical telecommunications band. The photonic band gap is marked with the yellow area in Figure 1c.

Photonic crystals have been proven to allow the propagation of surface states provided that they are properly terminated. To this end, the surface termination must break the lateral symmetry of the bulk periodic structure. Each termination provides different characteristics for the surface mode, and it is essentially a design element that controls the dispersion and the field distribution of the surface states. For the present design we choose to use two types of surface termination, termination **A** and termination **B**, which are schematically shown in Figure 1b.

DOI: 10.1021/acsphotonics.7b00739
ACS Photonics 2017, 4, 2782−2788

In both configurations we choose initially to omit the second row of the cylindrical air element and horizontally etch the whole structure at the middle of the external rods, creating in this way semicircles, as seen schematically in Figure 1b. We select the specific surface termination aiming at both facilitating an actual fabrication of the component and ensuring the efficiency of the desired electromagnetic operation. In that sense the second omitted row allows space for the implementation of additional rods necessary for the coupling of the dielectric dark surface states to outgoing radiation modes. At the same time it allows space for varying the diameter of the underlying rods as it happens for terminations **A** and **B**. In particular the diameter is equal to $D_A = D = 150$ nm for case **A** and $D_B = 300$ nm for case **B**. By modifying the diameters of the rods, the filling ratio, air:silicon area, changes and so does the dispersion of the surface mode. This control over the surfaces states is useful for achieving oblique beaming operation. Finally the semicircle cropped rods increase the wavelength range of the surface modes and further facilitate the coupling to the outgoing radiation.

The dispersion diagrams of the supported surface states for terminations **A** and **B** are presented in Figure 1c. They are calculated by solving the eigenvalue problem in a supercell with sufficiently large areas of surrounding air while imposing floquet periodic conditions at the external boundaries. Surface states lie within the photonic band gap, which is marked with the yellow area, and below the light line. Red curves correspond to surface modes of termination type **A**. The red solid line corresponds to the low-frequency, acoustic, surface mode, and the red dashed line corresponds to the high-frequency, optical, surface mode. The red solid branch is referred to as acoustic because it initiates from zeroing at the $k_x = 0$ edge of the Brillouin zone. In contrast, the optical modes of the red dashed branch are characterized by nonzero frequency at $k_x = 0$. The low-frequency surface state is pushed up by the dielectric band, and the optical surface state is pulled down from the air band. The high-frequency surface state is characterized by a small negative band slope (nearly flat), which translates in backward-propagating waves;[46] it is spectrally well separated from the acoustic surface state, and therefore we will not take it into account in the design. The acoustic surface mode **A** expands in a wavelength range of $\Delta\lambda = 220$ nm around the wavelength $\lambda = 1.52$ μm ($\alpha/\lambda_0 = 0.21$). The surface mode (acoustic) for termination **B** is shown in purple. It is the single supported surface state for termination **B**. The diameter of the underlying rods in termination **B** is increased with respect to case **A** (schematic in Figure 1b). As the air:silicon ratio of the second row in termination **B** increases, the surface mode is pushed to higher frequencies, approaching the light line. This is verified in Figure 1c, where we see that surface mode **B** expands in a wavelength range of $\Delta\lambda = 310$ nm around the wavelength $\lambda = 1.46$ μm ($\alpha/\lambda_0 = 0.219$). It is also noted here that the surface mode **B** does not overlap with the optical surface mode **A**. Finally, the distribution of the real part of the H_z component for the acoustic surface mode of termination **A** in a horizontally infinite structure, at wavelength $\lambda_0 = 1.5$ μm ($\alpha/\lambda_0 = 0.2125$), is presented in Figure 1d. It is observed that the surface wave stands bound to the interface of the two semi-infinite domains, that is, the photonic crystal and the air, and it decays exponentially in both domains away from the interface.

Coupling from Line-Defect Waveguide Modes to Oblique Directional Beams: Frequency Splitting Operation. One important motivation to invest in the manipulation of surface states is establishing a means of communication between the electromagnetic waves that travel through dielectric photonic crystal circuits and the outside world. Having designed the surface termination, we proceed by investigating the interaction between the terminating interface and a simple, straight line-defect waveguide. The line-defect waveguide is created by omitting an entire row/rows of air rods, which leads to the formation of a high-index slab surrounded by the reflective inverse photonic crystal. It is schematically shown in the inset of Figure 2. The width of the waveguide corresponds to the number of omitted rods and affects the characteristics of the propagating guided modes.

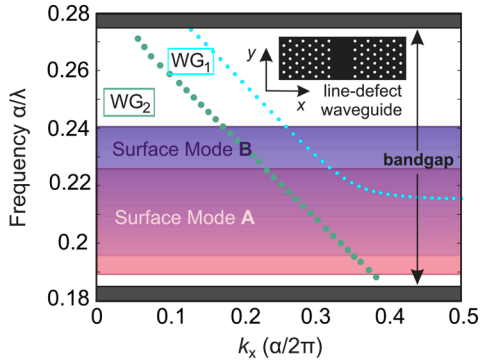

Figure 2. Dispersion diagram of the fundamental mode for the line-defect waveguide that feeds the surface mode. The schematic is shown in the inset. Light blue curve corresponds to the case of the waveguide of one rod width, WG_1, and the green curve corresponds to the case of five rod widths, WG_2. Gray-shaded areas delimit the photonic band gap of the infinite photonic crystal. The pink-shaded area corresponds to the surface mode **A** frequency regime, and the purple-shaded area corresponds to surface mode **B**. The dispersion of the corresponding surface states along k_x is shown in Figure 1c.

Figure 2 presents the dispersion diagram of the fundamental propagating modes for two line-defect waveguides of different width. Waveguide WG_1 corresponds to a line-defect of one omitted air rod and WG_2 to a waveguide of five omitted air rods. The propagating guided modes lie within the photonic band gap, which is delimited by the gray-shaded areas in Figure 2. Apart from the photonic band gap in Figure 2 we also mark the surface state spectrum. In particular, the wavelength regime of the surfaces mode is marked with the pink- and the purple-shaded area. The values are derived by the band diagrams of Figure 1c for modes **A** and **B**, respectively. We specifically mark this area, as for the coupling of the line-defect modes and the surface states we primarily need spectral overlap. As it is observed in Figure 2, the fundamental mode of the WG_1 waveguide does not extend to the whole spectrum of the band gap, and its spectral overlap with the surface modes is significantly small. This prohibits the use of the WG_1 waveguide for feeding the surface modes in a wide range of wavelengths. The spectral extent of the fundamental mode for the five-rod-width waveguide, WG_2, appears to serve our purpose better. In particular, the fundamental mode of WG_2, which is plotted with the green line in Figure 2, is very broadband (extends to the whole band gap) and exhibits a 100% overlap with the surface modes. Thus, using the five-rod-width line-defect waveguide, WG_2, and excitation with the fundamental mode is considered the optimum configuration for achieving surface state excitation and directional coupling operation.

DOI: 10.1021/acsphotonics.7b00739
ACS Photonics 2017, 4, 2782−2788

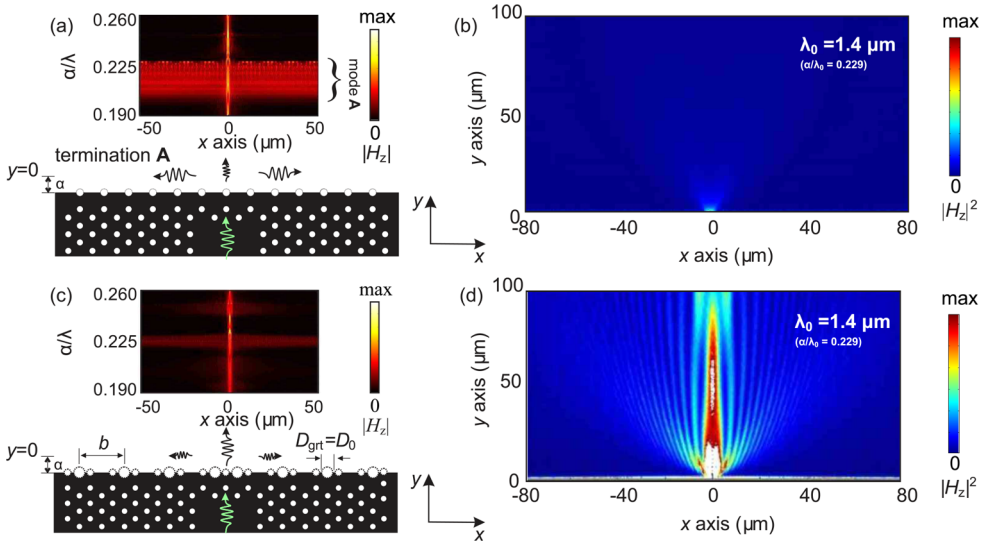

Figure 3. Line x-cross-section profile of the field intensity in the near field, which is at the exit of the terminating interface, within the range of α/λ = [0.195, 0.265] for the case of (a) surface termination of type **A** without additional scatterers and (c) surface termination of type **A** with additional scatterers. Corresponding schematics are also shown. Snapshots of the spatial energy distribution of the forward-propagating wave for the case of (b) surface termination of type **A** without additional scatterers and (b) surface termination of type **A** with additional scatterers. The wavelength of the operation is equal to λ_0 = 1.4 μm (α/λ = 0.229).

The WG_2 line-defect waveguide along with the terminating interface (termination of type **A**) is shown in the schematic of Figure 3a. The fundamental waveguide mode is excited at the input port and the wave travels in the ΓK (k_x = 0, $k_y \neq 0$) direction toward the photonic crystal/air interface. At this point the waveguide energy is scattered generating waves with nonzero k_x components that are partially coupled to the surface waves propagating in the ΓM ($k_x \neq 0$, k_y = 0) direction and partially converted into a free-space spherical wave leaking from the waveguide effective aperture. That is, the coupling is a result of the waveguide and the termination intersection that breaks both the vertical and lateral symmetry. The final goal is the generation of a well-defined outgoing beam from the surface mode, and it is achieved by increasing the effective width of the grating and by minimizing the waveguide aperture leakage versus the surface mode. In order to enhance the energy transfer from the waveguide mode to the surface waves, we introduce an intermediate coupling element. The intermediate coupling element lies inside the waveguide and close to the terminating area. It consists of five additional scatterers that intervene between the surface termination and the line-defect waveguide: one row of two holes and one row of three holes. This region acts as an impedance matching element between the waveguide and the termination. It has been found to increase the surface propagating energy with respect to the forward leakage, but, at the same time, it also increases the return losses in the feeding waveguide. This consequently leads to the deterioration of the overall coupling efficiency. In fact, in the present designs the return losses are on average as high as 60%. Evidently there is interplay between the coupling losses and the quality of the outgoing beams. Given that the focus is on the latter, we consider that the increase of the overall coupling losses is a fair trade-off for the quality of the beams. Further optimization may be possible.

We investigate, initially, the excitation of the surface states in the structure with solely termination of type **A**, which is without any additional grating scatterers. In particular we record the x-cross-section profile of the field intensity in the near field within a wavelength range of α/λ = [0.19, 0.26]. The results are presented in Figure 3a. The profiles are calculated at the exit of the terminating interface, that is, at y = 0 (which corresponds to a distance of α from the termination), and extends in the range [−50 μm, 50 μm] along the x-axis. As seen in Figure 3a, in the wavelength range where the surface mode is excited, the energy spreads along the photonic crystal−air interface and less energy goes in the forward direction. Figure 3b shows a snapshot of the energy distribution of the wave that exits the structure at the wavelength of λ_0 = 1.4 μm (α/λ = 0.229). The absence of a collimated beam is verified. The next step is to add, symmetrically in both exit sides, the additional scatterers, as shown in the schematic of Figure 3c. The additional scatterers, also referred to as grating modulation, facilitate the coupling of the dark surface states into outgoing radiation. In particular, the interaction of the surface wave and the scatterer generates diffracted waves with nonzero wave vector components that interfere constructively in the forward direction.[23] The shape and the periodicity of the grating modulation is designed with respect to the fabrication feasibility. Thus, each scatterer is a semicircle air hole of diameter $D_{grt} = D_0$ = 340 nm arranged in periodicity $b = 2\alpha\sqrt{3}$. The value of the periodicity provides sufficient momentum for the surface wave to couple to radiation (the surface wave−diffraction equation should assume real solutions[28,47]). For the grating-modulated structure we calculate the x-cross-section profile of the near-field intensity in the range λ = [1.23, 1.68] (α/λ = [0.19, 0.26]), seen in Figure 3c. Contrary to Figure 3a, we now observe that the intensity of the surface wave decreases while the intensity of the field at the center exit of the structure is enhanced. Figure 3d presents a snapshot of the energy distribution of the exiting wave at the wavelength of λ_0 = 1.4 μm (α/λ = 0.229). In this case the sideways-propagating surface wave interacts with the periodic scatterers and undergoes successive diffractions. This leads to the formation of the narrow high directional beam in the forward direction. In summary, Figure 3 describes the way that the spread of the beam that exits the line-defect waveguide depends on the surface termination.

DOI: 10.1021/acsphotonics.7b00739
ACS Photonics 2017, 4, 2782−2788

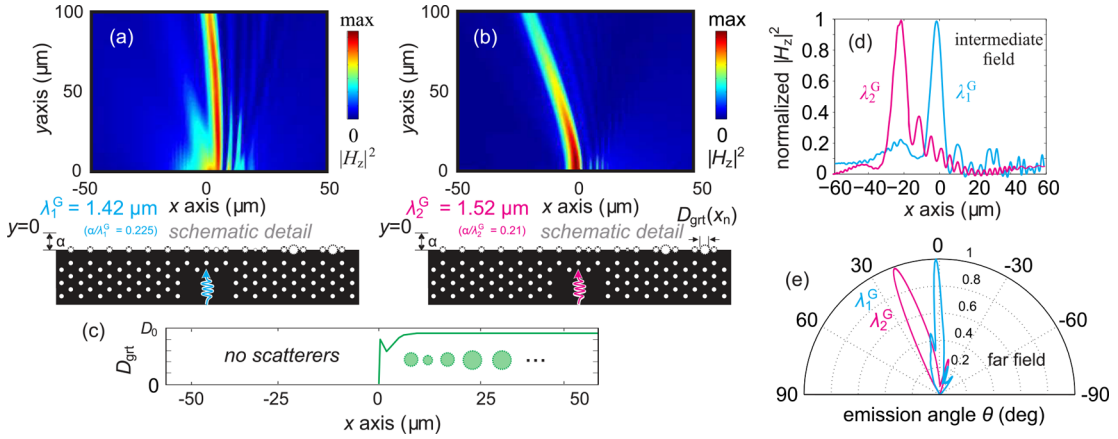

Figure 4. Case of a single-sided grating modulation. (a) Energy distribution of the outgoing field in the near- and intermediate-field region at λ_1^G = 1.42 μm (α/λ_1^G = 0.225) and schematic detail of the structure. (b) Energy distribution of the outgoing field in the near- and intermediate-field region at λ_2^G = 1.52 μm (α/λ_2^G = 0.21) and schematic detail of the structure. (c) Scatterer diameter modulation D_{grt} along the x-axis. (d) Comparison of the beam spatial distribution in the near- and intermediate-field region at wavelength λ_1^G = 1.42 μm (α/λ_1^G = 0.225) and λ_2^G = 1.52 μm (α/λ_2^G = 0.21). (e) Comparison of the beam spatial distribution in the far-field region at wavelength λ_1^G = 1.42 μm (α/λ_1^G = 0.225) and λ_2^G = 1.52 μm (α/λ_2^G = 0.21).

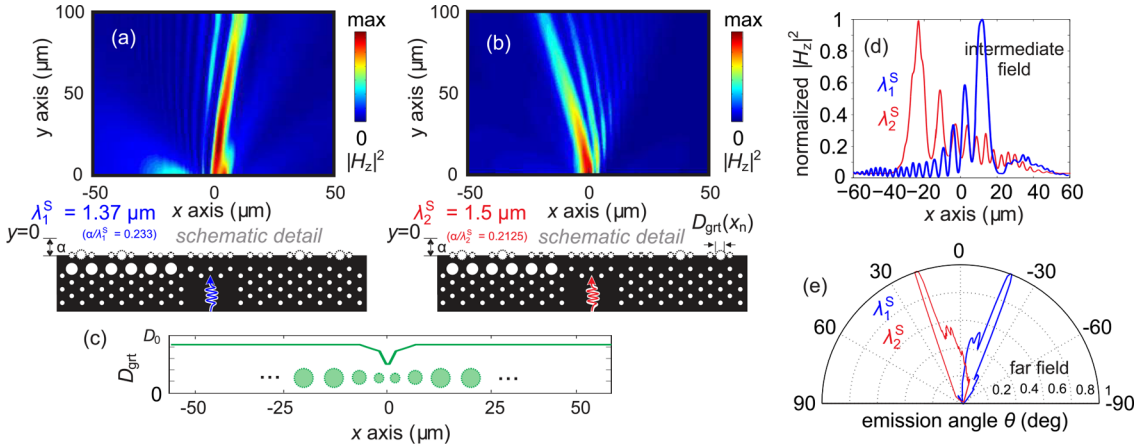

Figure 5. Case of an asymmetric surface termination. (a) Energy distribution of the outgoing field in the near- and intermediate-field region at λ_1^S = 1.37 μm (α/λ_1^S = 0.233) and schematic detail of the structure. (b) Energy distribution of the outgoing field in the near- and intermediate-field region at λ_2^S = 1.5 μm (α/λ_2^S = 0.2125) and schematic detail of the structure. (c) Scatterer diameter modulation D_{grt} along the x-axis. (d) Comparison of the beam spatial distribution in the near- and intermediate-field region at wavelength λ_1^S = 1.37 μm (α/λ_1^S = 0.233) and λ_2^S = 1.5 μm (α/λ_2^S = 0.2125). (e) Comparison of the beam spatial distribution far-field region at wavelengths λ_1^S = 1.37 μm (α/λ_1^S = 0.233) and λ_2^S = 1.5 μm (α/λ_2^S = 0.2125).

In the case of Figure 3 the symmetry of the surface termination and the grating with respect to the waveguide leads to beam emission along the forward direction, the y-axis. Off-axis directional emission can be achieved when one breaks this symmetry. In ref 28 we have demonstrated experimentally a dielectric rod photonic crystal configuration that provides off-axis emission and frequency splitting operation in the microwave regime. Given the fabrication restrictions in the present air-holes-in-Si inverse photonic crystal structure, we choose to follow two alternative paths to achieve beam steering and frequency splitting for the infrared and optical regime. The first oblique beaming implementation is presented in the schematic of Figure 4a and b. It consists of the line-defect waveguide, the intermediate coupling element, and an asymmetric grating layer. In particular only one exit side (right) hosts scatterers, while the other side contains only the surface termination of type **A**. In this design, the absence of grating scatterers on one side of the termination leads to nondirectional leakage from the surface propagating wave and is expected to further increase the overall coupling losses. To reduce the impedance mismatch and optimize the quality of the outgoing beams, the diameter of the grating scatterers is variable along the x-axis. The optimized function of the scatterers' diameter $D_{grt} = D_{grt}(x_n)$, where $x_n = nb$ and $n = [0 \ldots 50]$, is presented in Figure 4c. Figure 4a presents the spatial distribution of the energy emerging from the structure at the wavelength λ_1^G = 1.42 μm (α/λ_1^G = 0.225). A well-defined beam at an angle of θ_1^G = +1 deg from the forward direction is observed. Close to the exit of the structure, in the near-field regime, we observe the existence of side lobes (to the right) and an unshaped scattered lobe (to left) that does not propagate significantly to the intermediate field and far field (seen in Figure 4e). Figure 4b presents the spatial distribution of the energy emerging from the structure at the wavelength λ_2^G = 1.52 μm (α/λ_2^G = 0.21). A well-defined beam at an angle of θ_2^G = +23 deg from the forward direction is observed. Here, the side lobes are suppressed. Figure 4d presents the comparison of the spatial distribution of the outgoing energy in an x-cross-section of the intermediate field regime (y = 100 μm). The blue curve corresponds to the λ_1^G = 1.42 μm (α/λ_1^G = 0.225) directional

DOI: 10.1021/acsphotonics.7b00739
ACS Photonics 2017, 4, 2782−2788

emission (Figure 4a), and the magenta curve corresponds to the λ_2^G = 1.52 μm (α/λ_2^G = 0.21) directional emission (Figure 4b). The beams are well-defined and exhibit low spatial overlap. The comparison of the far-field radiation for the two wavelengths is presented in Figure 4e. The far-field radiation is well-defined, and the two beams exhibit an angular separation of $\Delta\theta^G$ = 22 deg and spectral separation of $\Delta\lambda^G$ = 100 nm.

An alternative way to achieve oblique directionality of the outgoing beam in this photonic crystal component is by implementing the structure presented in the schematics of Figure 5a and b. It consists of the line-defect waveguide, the intermediate coupling component, an asymmetric surface termination of type **A** and **B**, and a symmetric (both sides) grating configuration. Again, to reduce the impedance mismatch and optimize the quality of the outgoing beams, the diameter of the grating scatterers is modulated along the *x*-axis, as seen in Figure 5c. The asymmetric surface corrugation supports the propagation of surface modes with different dispersion, as can be derived by the diagrams of Figure 1c. At a certain wavelength the ratio k_x/k_0 is different for termination **A** and **B**,[47] in Figure 1c curves with red and purple, respectively, and each side is expected to generate constructive interference in different directions for each particular wavelength. The spatial distribution of the energy emerging from the structure at wavelengths λ_1^S = 1.37 μm (α/λ_1^S = 0.233) and λ_2^S = 1.5 μm (α/λ_2^S = 0.2125) is presented in Figure 5a and b, respectively. In both cases we observe well-defined emerging beams at angles θ_1^S = +20 deg and θ_2^S = −23 deg from the forward direction. The comparison of the *x*-cross-section spatial distribution of the outgoing energy in the intermediate-field regime (y = 100 μm) is presented in Figure 5d. The two beams are spatially well separated, with angular separation $\Delta\theta^S$ = 43 deg, while their spectral separation is $\Delta\lambda^S$ = 130 nm. The far-field radiation patterns for the two wavelengths are presented in Figure 5e, where we observe two well-defined and separated beams. Compared to the previous implementation, presented in Figure 4, we observe that the performance of the asymmetric surface termination implementation, presented in Figure 5, slightly deteriorates. In particular the side lobes of the emerging beams presented in Figure 5d and e are enhanced, which is a result of the strong grating scattering and the increased impedance mismatch between the various elements of the components. Nevertheless, for the two wavelengths of the optical telecommunications band, the beams exhibit sufficiently enhanced spatial and spectral separation.

Conclusions. We have presented a frequency splitting dielectric structure designed for operation in the near-infrared, telecom optical band and optical regime. The structure is based on dielectric air-holes-in-Si inverse photonic crystals made of an electromagnetically infinitely thick Si slab perforated with air holes in a standard triangular arrangement. It consists of a line-defect waveguide that feeds a surface termination designed to sustain the propagation of dark, surface states. Additional surface modulation grating provides the coupling of the surface states to outgoing radiation of controllable directionality. Different surface terminations are discussed and analyzed. The structures provide well-defined beams with enhanced spectral and spatial isolation and can serve as frequency splitters. The designs comply with the currently used materials and fabrication methods concerning the treatment of dielectric periodic media for operation in the near-infrared and optical regime.

AUTHOR INFORMATION

Corresponding Author

*E-mail: atasolam@iesl.forth.gr.

ORCID

Anna C. Tasolamprou: 0000-0003-4652-5470

Notes

The authors declare no competing financial interest.

ACKNOWLEDGMENTS

This work was supported by the European Research Council under ERC Advanced Grant No. 320081 (PHOTOMETA). Work at Ames Laboratory was partially supported by the U.S. Department of Energy (Basic Energy Sciences, Division of Materials Sciences and Engineering) under Contract No. DE-AC02-07CH11358.

REFERENCES

(1) Yablonovitch, E. Inhibited spontaneous emission in solid-state physics and electronics. *Phys. Rev. Lett.* **1987**, *58*, 2059−2062.

(2) Joannopoulos, J. D.; Villeneuve, P. R.; Fan, S. Photonic crystals: Putting a new twist on light. *Nature* **1997**, *386*, 143−149.

(3) Ho, K. M.; Chan, C. T.; Soukoulis, C. M.; Biswas, R.; Sigalas, M. Photonic band gaps in three dimensions: New layer-by-layer periodic structures. *Solid State Commun.* **1994**, *89*, 413−416.

(4) Soukoulis, C. M.; Wegener, M. Past achievements and future challenges in the development of three-dimensional photonic metamaterials. *Nat. Photonics* **2011**, *5*, 523−530.

(5) Meade, R. D.; Brommer, K. D.; Rappe, A. M.; Joannopoulos, J. D. Electromagnetic Bloch waves at the surface of a photonic crystal. *Phys. Rev. B: Condens. Matter Mater. Phys.* **1991**, *44*, 10961−10964.

(6) Economou, E. N. Surface plasmons in thin films. *Phys. Rev.* **1969**, *182*, 539−554.

(7) Arjavalingam, G.; Robertson, W. M.; Meade, R. D.; Brommer, K. D.; Rappe, A. M.; Joannopoulos, J. D. Observation of surface photons on periodic dielectric arrays. *Opt. Lett.* **1993**, *18*, 528−530.

(8) Ramos-Mendieta, F.; Halevi, P. Surface modes in a 2D array of square dielectric cylinders. *Solid State Commun.* **1996**, *100*, 311−314.

(9) Martín-Moreno, L.; Garcia-Vidal, F. J.; Lezec, H. J.; Degiron, A.; Ebbesen, T. W. Theory of highly directional emission from a single subwavelength aperture surrounded by surface corrugations. *Phys. Rev. Lett.* **2003**, *90*, 167401.

(10) Lezec, H. J.; Degiron, A.; Devaux, E.; Linke, R. A.; Martin-Moreno, L.; Garcia-Vidal, F. J.; Ebbesen, T. W. Beaming Light from a Subwavelength Aperture. *Science* **2002**, *297*, 820−822.

(11) Caglayan, H.; Ozbay, E. Surface wave splitter based on metallic gratings with sub-wavelength aperture. *Opt. Express* **2008**, *16*, 19091−19096.

(12) Dai, W.; Soukoulis, C. M. Control of beaming angles via a subwavelength metallic slit surrounded by grooves. *Phys. Rev. B: Condens. Matter Mater. Phys.* **2010**, *82*, 045427.

(13) Lu, C.; Liu, Y.-C.; Hu, X.; Yang, H.; Gong, Q. Integrated ultracompact and broadband wavelength demultiplexer based on multi-component nano-cavities. *Sci. Rep.* **2016**, *6*, 27428.

(14) Wang, B.; Dai, W.; Fang, A.; Zhang, L.; Tuttle, G.; Koschny, T.; Soukoulis, C. Surface waves in photonic crystal slabs. *Phys. Rev. B: Condens. Matter Mater. Phys.* **2006**, *74*, 195104.

(15) Dyakov, S. A.; Baldycheva, A.; Perova, T. S.; Li, G. V.; Astrova, E. V.; Gippius, N. A.; Tikhodeev, S. G. Surface states in the optical spectra of two-dimensional photonic crystals with various surface terminations. *Phys. Rev. B: Condens. Matter Mater. Phys.* **2012**, *86*, 115126.

(16) Hsu, C. W.; Zhen, B.; Chua, S. L.; Johnson, S. G.; Joannopoulos, J. D.; Soljačić, M. Bloch surface eigenstates within the radiation continuum. *Light: Sci. Appl.* **2013**, *2*, e84.

DOI: 10.1021/acsphotonics.7b00739
ACS Photonics 2017, 4, 2782−2788

(17) Erim, M. N.; Erim, N.; Kurt, H. Optical surface modes of photonic crystals for dual-polarization waveguide. *Phot. Nano. Fundam. Appl.* **2013**, *11*, 123−131.
(18) Dai, W.; Soukoulis, C. M. Converging and wave guiding of Gaussian beam by two-layer dielectric rods. *Appl. Phys. Lett.* **2008**, *93*, 201101.
(19) Tasolamprou, A. C.; Zhang, L.; Kafesaki, M.; Koschny, T.; Soukoulis, C. M. Experimentally excellent beaming in a two-layer dielectric structure. *Opt. Express* **2014**, *22*, 23147−23152.
(20) Cheng, Y.; Redondo, J.; Staliunas, K. Beam focusing in reflections from flat subwavelength diffraction gratings. *Phys. Rev. A: At., Mol., Opt. Phys.* **2014**, *89*, 033814.
(21) Cheng, Y.; Zeng, H.; Trull, J.; Cojocaru, C.; Malinauskas, M.; Jukna, T.; Wiersma, D.; Staliunas, K. Beam focalization in reflection from flat dielectric subwavelength gratings. *Opt. Lett.* **2014**, *39*, 6086−6089.
(22) Bulu, I.; Caglayan, H.; Ozbay, E. Beaming of light and enhanced transmission via surface modes of photonic crystals. *Opt. Lett.* **2005**, *30*, 3078−3080.
(23) Moussa, R.; Wang, B.; Tuttle, G.; Koschny, T.; Soukoulis, C. Effect of beaming and enhanced transmission in photonic crystals. *Phys. Rev. B: Condens. Matter Mater. Phys.* **2007**, *76*, 235417.
(24) Moreno, E.; Garcia-Vidal, F. J.; Martin-Moreno, L. Enhanced transmission and beaming of light via photonic crystal surface modes. *Phys. Rev. B: Condens. Matter Mater. Phys.* **2004**, *69*, 121402.
(25) Kramper, P.; Agio, M.; Soukoulis, C. M.; Birner, A.; Müller, F.; Wehrspohn, R. B.; Gösele, U.; Sandoghdar, V. Highly Directional Emission from Photonic Crystal Waveguides of Subwavelength Width. *Phys. Rev. Lett.* **2004**, *92*, 113903.
(26) Morrison, S. K.; Kivshar, Y. S. Engineering of directional emission from photonic-crystal waveguides. *Appl. Phys. Lett.* **2005**, *86*, 1−3.
(27) Caglayan, H.; Bulu, I.; Ozbay, E. Off-axis directional beaming via photonic crystal surface modes. *Appl. Phys. Lett.* **2008**, *92*, 092114.
(28) Tasolamprou, A. C.; Zhang, L.; Kafesaki, M.; Koschny, T.; Soukoulis, C. M. Frequency splitter based on the directional emission from surface modes in dielectric photonic crystal structures. *Opt. Express* **2015**, *23*, 13972−13982.
(29) Hayran, Z.; Turduev, M.; Botey, M.; Herrero, R.; Staliunas, K.; Kurt, H. Numerical and experimental demonstration of a wavelength demultiplexer design by point-defect cavity coupled to a tapered photonic crystal waveguide. *Opt. Lett.* **2016**, *41*, 119−122.
(30) Momeni, B.; Huang, J.; Soltani, M.; Askari, M.; Mohammadi, S.; Rakhshandehroo, M.; Adibi, A. Compact wavelength demultiplexing using focusing negative index photonic crystal superprisms. *Opt. Express* **2006**, *14*, 2413−2422.
(31) Chung, K. B.; Hong, S. W. Wavelength demultiplexers based on the superprism phenomena in photonic crystals. *Appl. Phys. Lett.* **2002**, *81*, 1549−1551.
(32) Goyal, A.; Dutta, H.; Pal, S. Recent advances and progress in photonic crystal-based gas sensors. *J. Phys. D: Appl. Phys.* **2017**, *50*, 203001.
(33) Piggott, A.; Lu, J.; Lagoudakis, K.; Petykiewicz, J.; Babinec, T.; Vucković, J. Inverse design and demonstration of a compact and broadband on-chip wavelength demultiplexer. *Nat. Photonics* **2015**, *9*, 374−377.
(34) Angelini, A.; Munzert, P.; Enrico, E.; De Leo, N.; Scaltrito, L.; Boarino, L.; Giorgis, F.; Descrovi, E. Surface-Wave-Assisted Beaming of Light Radiation from Localized Sources. *ACS Photonics* **2014**, *1*, 612−617.
(35) Shibanuma, T.; Matsui, T.; Roschuk, T.; Wojcik, J.; Mascher, P.; Albella, P.; Maier, S. Experimental Demonstration of Tunable Directional Scattering of Visible Light from All-Dielectric Asymmetric Dimers. *ACS Photonics* **2017**, *4*, 489−494.
(36) Wijnhoven, J. E. G. J.; Vos, W. L. Preparation of photonic crystals made of air spheres in titania. *Science* **1998**, *281*, 802−804.
(37) Combrie, S.; De Rossi, A.; Tran, Q. V.; Benisty, H. GaAs photonic crystal cavity with ultrahigh Q: Microwatt nonlinearity at 1.55 μm. *Opt. Lett.* **2008**, *33*, 1908−1910.
(38) Vućković, J.; Pelton, M.; Scherer, A.; Yamamoto, Y. Optimization of three-dimensional micropost microcavities for cavity quantum electrodynamics. *Phys. Rev. A: At., Mol., Opt. Phys.* **2002**, *66*, 1−9.
(39) Grishina, D. A.; Harteveld, C. A. M.; Woldering, L. A.; Vos, W. L. Method for making a single-step etch mask for 3D monolithic nanostructures. *Nanotechnology* **2015**, *26*, 505302.
(40) Krauss, T. F.; De La Rue, R. M.; Brand, S. Two-dimensional photonic-bandgap structures operating at near-infrared wavelengths. *Nature* **1996**, *383*, 699−702.
(41) Loncar, M.; Doll, T.; Vućković, J.; Scherer, A. Design and fabrication of silicon photonic crystal optical waveguides. *J. Lightwave Technol.* **2000**, *18*, 1402−1411.
(42) Huisman, S. R.; Ctistis, G.; Stobbe, S.; Mosk, A. P.; Herek, J. L.; Lagendijk, A.; Lodahl, P.; Vos, W. L.; Pinkse, P. W. H. Measurement of a band-edge tail in the density of states of a photonic-crystal waveguide. *Phys. Rev. B: Condens. Matter Mater. Phys.* **2012**, *86*, 155154.
(43) Huisman, S. R.; Nair, R. V.; Woldering, L. A.; Leistikow, M. D.; Mosk, A. P.; Vos, W. L. Signature of a three-dimensional photonic band gap observed on silicon inverse woodpile photonic crystals. *Phys. Rev. B: Condens. Matter Mater. Phys.* **2011**, *83*, 205313.
(44) Woldering, L. A.; Mosk, A. P.; Vos, W. L. Design of a three-dimensional photonic band gap cavity in a diamondlike inverse woodpile photonic crystal. *Phys. Rev. B: Condens. Matter Mater. Phys.* **2014**, *90*, 115140.
(45) Joannopoulos, J. D.; Johnson, S. G.; Winn, J. N.; Meade, R. D. *Photonic Crystals: Molding the Flow of Light*, Second Edition, Princeton University Press; 2011.
(46) Foteinopoulou, S.; Kafesaki, M.; Economou, E. N.; Soukoulis, C. M. Backward surface waves at photonic crystals. *Phys. Rev. B: Condens. Matter Mater. Phys.* **2007**, *75*, 245116.
(47) The direction of the outgoing radiation is described by the surface wave−diffraction equation $k_{spp} + N\frac{2\pi}{b} = k_0 \sin\theta$ where k_{spp} is the surface wave wavevector assuming an infinite undistorted surface termination, θ is the direction of the outgoing beam, and N is the spatial harmonic index that denotes the grating order.

DOI: 10.1021/acsphotonics.7b00739
ACS Photonics 2017, 4, 2782−2788